Science Advances

AAAS

Supplementary Materials for

Maximizing efficiency of dipolar recoupling in solid-state NMR using optimal control sequences

Zdeněk Tošner*, Matthias J. Brandl, Jan Blahut, Steffen J. Glaser, Bernd Reif*

*Corresponding author. Email: zdenek.tosner@natur.cuni.cz (Z.T.); reif@tum.de (B.R.)

The PDF file includes:

Other Supplementary Material for this manuscript includes the following:

Theoretical background of optimal control calculations and rescaling property

In this section, we briefly outline the necessary theory for the calculations used in our study. Besides spin dynamics, we summarize the optimal control procedures used to design new pulse sequences to facilitate the discussion and to adapt optimal control experiments to a range of MAS frequencies.

We base our analysis on the irreducible spherical tensor formalism which is convenient to describe rotations of spherical tensor operators (51). The total NMR Hamiltonian can be split into an internal part, H_{int}, which includes the chemical shielding, dipolar and J-coupling interactions (possibly also the quadrupolar interaction), and an external part, H_{RF}, describing the influence of radiofrequency (rf) irradiation. The calculations are conducted in the reference frame which rotates around the axis given by the direction of an external static magnetic field with a frequency equal to the Larmor frequency of the spins. In addition, the secular approximation is assumed, and the Hamiltonians can be written as

$$H(t) = H_{\text{int}}(t) + H_{\text{RF}}(t) \tag{1}$$

$$H_{\text{RF}}(t) = \sum_i \omega_{i,x}^{\text{RF}}(t) I_{i,x} + \omega_{i,y}^{\text{RF}}(t) I_{i,y} \tag{2}$$

$$H_{\text{int}}(t) = \sum_\lambda A_{0,0}^{\lambda,\text{LAB}} T_{\text{iso}}^\lambda + \sum_\lambda T_{\text{aniso}}^\lambda \sum_{r=-2}^{+2} \omega_{(r)}^\lambda \, e^{-ir\omega_{\text{R}}t} \tag{3}$$

$$\omega_{(r)}^\lambda = \sum_{p,q=-2}^{+2} A_{2,p}^{\lambda,\text{PAS}} D_{p,q}^{(2)}\big(\Omega_{\text{PAS}}^{\text{CRY}}\big) D_{q,r}^{(2)}\big(\Omega_{\text{CRY}}^{\text{ROT}}\big) d_{r,0}^{(2)}(\beta_{\text{RL}}) \tag{4}$$

The rf Hamiltonian $H_{\text{RF}}(t)$ involves external manipulations in terms of rf irradiation. In Eq. 2, it is expressed as a sum over x- and y-phase contributions for the involved spins (or spin species) through the functions $\omega_{i,x}^{\text{RF}}(t)$ and $\omega_{i,y}^{\text{RF}}(t)$. These functions constitute the actual rf pulse sequence and are optimized in the optimal control procedure.

The internal Hamiltonian $H_{\text{int}}(t)$ in Eq. 3 is split into the time independent isotropic part, and the time dependent anisotropic part expressed as a Fourier series with the interaction amplitudes $\omega_{(r)}^\lambda$ defined in Eq. 4. The symbol $A_{l,q}^{\lambda,\text{PAS}}$ denotes the component q of the rank-l spatial tensor corresponding to the interaction λ, and is expressed in the principal axis system (PAS) (51). $A_{l,q}^{\lambda,PAS}$ is transformed via the crystal-fixed frame (CRY) and the rotor-fixed frame (ROT) into the laboratory frame (LAB) using rank-2 Wigner coefficients $D_{p,q}^{(2)}(\Omega)$, using the Euler angles $\Omega_{\text{PAS}}^{\text{CRY}}, \Omega_{\text{CRY}}^{\text{ROT}}$ and $\Omega_{\text{ROT}}^{\text{LAB}}$ which describe the relative orientations of these reference systems. For powder samples, the distribution of crystallite orientations is reflected in the distribution of the Euler angles $\Omega_{\text{CRY}}^{\text{ROT}}$. The MAS condition implies that the transformation from ROT to LAB is time dependent and can be expanded using $\Omega_{\text{ROT}}^{\text{LAB}}(t) = (\omega_{\text{R}}t, \beta_{\text{RL}}, 0)$, where ω_{R} denotes the angular frequency of the rotor, and β_{RL} is the magic angle ($\beta_{\text{RL}} = \text{atan}\sqrt{2}$). The terms T_{iso}^λ and T_{aniso}^λ represent spin operators of isotropic and anisotropic parts of the respective interactions (51).

For numerical calculations, the time dependence of the Hamiltonian is approximated by assuming a piecewise constant function, which can be obtained by sampling the total Hamiltonian at times t_k separated by intervals Δt, $t_k = k\Delta t$, $k = 0, 1, \ldots N$. A convenient choice of Δt is based on the MAS frequency, $\Delta t = (1/M) \cdot (2\pi/\omega_R)$, where M is the number of time steps within one rotor period, as it allows to keep synchronization with the sample rotation *(52-54)*. The spin dynamics of an NMR experiment can then be expressed in terms of the density matrix operator, $\rho(t_k)$, evolving under the influence of the propagators $U_k(t_{k-1}, t_k)$ extending the evolution by the time interval Δt. At the end of the pulse sequence, $T = N\Delta t$, we have

$$\rho(T) = U_N \ldots U_2 U_1 \rho(0) U_1^\dagger U_2^\dagger \ldots U_N^\dagger \tag{5}$$

$$U_k = \exp\{-i[H_{\text{int}}(t_k) + H_{\text{RF}}(t_k)]\Delta t\} \tag{6}$$

We set up a numerical optimization protocol to find the series of rf amplitudes $\omega_{i,\alpha}^{\text{RF}}(t_k)$ that constitute the total pulse sequence and provide the maximal transfer efficiency for a desired magnetization transfer process. The optimal control algorithm GRAPE (*19*) was implemented in the software package SIMPSON (*41, 46, 47*) to achieve this goal. Typically, a state-to-state transfer of magnetization from one nucleus to another represented by the initial state $\rho(0)$ and the final state F at time $t = T$ is optimized using the target function

$$\Phi = \sum_i w_i \Phi_i \tag{7}$$

$$\Phi_{\text{i}} = Tr\,\{F^\dagger U(0,T)\rho(0)U^\dagger(0,T)\} \tag{8}$$

Optimal control theory provides easy access to the first derivative of the objective function Φ_i and allows to optimize tens of thousands of variables – rf pulse amplitudes and phases – at once. The summation over i in Eq. 7 reflects the fact that the calculation is performed for a particular set of parameters like the orientation of one crystallite within a powder sample. Because the pulse sequence is required to work for all possible crystallite orientations, independent calculations are repeated for a representative set of orientations. The total target function is a sum weighted by the relative contributions w_i of each orientation. Additionally, specific experimental conditions such as the distribution of chemical shifts or the rf field inhomogeneity distribution within the sample can be covered as well. Eq. 7 allows to introduce these conditions easily by increasing the sum.

We show below that tm-SPICE sequences can be adapted for a different MAS frequency ω_R^{new} according to the following protocol. Using a scaling factor

$$\xi = \omega_R^{\text{new}}/\omega_R^{\text{opt}} \tag{9}$$

the new pulse shape is obtained by adjusting

1. length of the shape: $T_{\text{new}} = T/\xi$
2. rf amplitudes of the shape: $\omega_1^{\text{new}} = \omega_1^{\text{opt}} \cdot \xi$

We define new time steps as $t'_k = k\Delta t'$, where $\Delta t' = (1/M) \cdot (2\pi/\omega_{\mathrm{R}}^{\mathrm{new}})$ and $k = 1, \dots N$. At the time t'_k, the rotor attains the same orientation as during the time t_k defined previously with the frequency $\omega_{\mathrm{R}}^{\mathrm{opt}}$, as it is schematically depicted in Figure S-1. We also have $\Delta t' = \Delta t/\xi$, thus the rf pulses are again synchronized with the sample rotation.
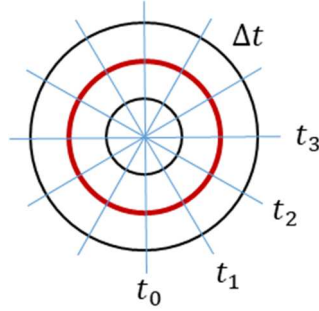
Figure S-1. Representation of the time steps used in the numerical simulation of a MAS experiment. The length of each circle represents one rotor period, the red color indicates the nominal MAS frequency. When the frequency is larger, the rotor period is shorter, and it corresponds to the inner circle. The relative phase of the rotor is the same at times t_k.

The central argument, that optimal control sequences can be adjusted to different MAS frequencies and keep their efficiency, is based on the fact that the propagators U_k, Eq. 6, remain the same upon a change of the MAS frequency. The exponent contains the terms $H_{\mathrm{int}}(t_k)\Delta t$ and $H_{\mathrm{RF}}(t_k)\Delta t$. By rescaling the rf amplitudes $\omega_x^{\mathrm{RF}}(t)$, $\omega_y^{\mathrm{RF}}(t)$ with the factor ξ, the new rf Hamiltonian $H'_{\mathrm{RF}}(t'_k)$ satisfies $H'_{\mathrm{RF}}(t'_k)\Delta t' = H_{\mathrm{RF}}(t_k)\Delta t$, ensuring that this part of the propagator exponent is identical – the effect of the pulses is unchanged, the same effective angle is achieved. In case of the term $H_{\mathrm{int}}(t_k)\Delta t$, the situation is more complex. By rescaling the time increments, we ensure the same sampling of the time modulations of the interactions, $H_{\mathrm{int}}(t'_k) = H_{\mathrm{int}}(t_k)$. However, the resulting propagators U_k are different since $\Delta t' \neq \Delta t$. We note that we designed our pulse sequence to work equally well for all possible crystallite orientations, i.e., different conditions in Eq. 7. This powder distribution, which is imposed by the Euler angles $\Omega_{\mathrm{CRY}}^{\mathrm{ROT}}$, leads to a distribution of the effective interaction amplitudes, Eq. 4. If we assume that only a dipole-dipole interaction contributes, the effective amplitudes d_{eff} for different crystallite orientations will be within the interval $[0, d_{\mathrm{max}}]$ and they will be modulated by sample rotation as depicted in Figure S-2. Similarly, the ratio $\Delta t'/\Delta t$ can be regarded as a scaling factor of the effective interaction amplitudes.
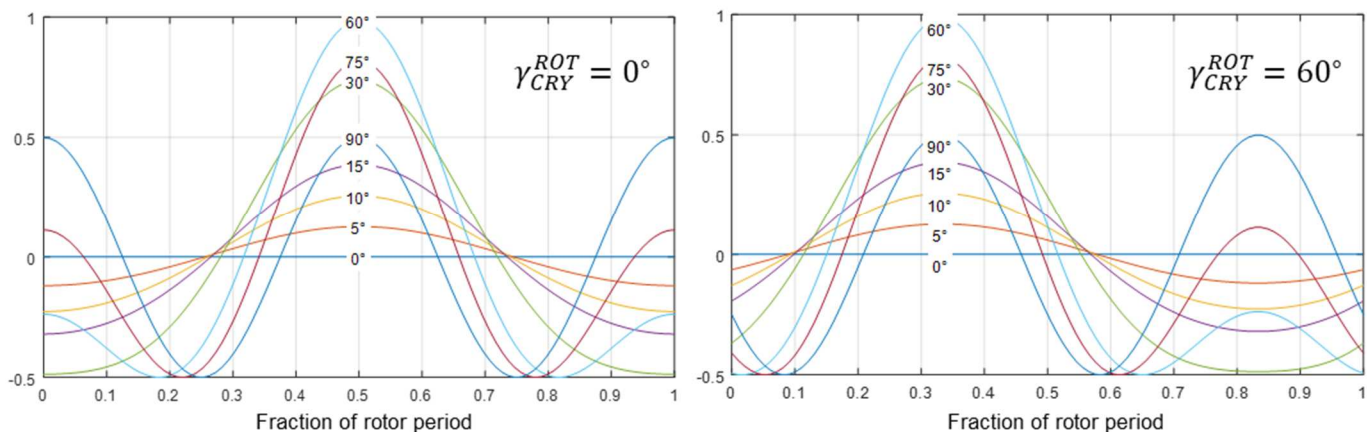
Figure S-2. Dependence of the effective dipolar coupling d_{eff} on crystallite orientation and on sample rotation, evaluated using Equations 3 and 4, $d_{\text{eff}}(t) = \sum_{r=-2}^{+2} \omega_{(r)}^{\lambda} e^{-ir\omega_R t}$. Different curves correspond to different crystallite angles β_{CRY}^{ROT} with values indicated at each curve. The horizontal axis represents time as a fraction of one rotor period. At different crystallites, the effective coupling is scaled by an amount depending on the orientation of the inter-nuclear vector with respect to the rotor axis (i.e., angle β_{CRY}^{ROT}) and it is periodically modulated in time as the sample rotates. The initial phase of these modulations depends on the crystallite angle γ_{CRY}^{ROT}. This phase can be absorbed into the rotor phase.

After rescaling, the propagator U_k will be thus identical to another original propagator corresponding to a different crystallite orientation. This is true for $1/\xi < 1$, i.e., for transformation to higher MAS frequencies. When going to $\omega_R^{\text{new}} < \omega_R^{\text{opt}}$, propagators with $d_{\text{eff}} > d_{\text{max}}$ will not find their counterparts in the original set, which will lead to a decreased performance of the pulse sequence. When several anisotropic interactions are present, with different orientations of their principal axis systems, the internal Hamiltonian H_{int} evaluated for a particular crystallite orientation might not simply be a scaled version of H_{int} taken at a different orientation. Thus, a decreased performance should be expected.

Optimal control sequences are typically optimized to include robustness towards a distribution of the isotropic (time independent) interactions like chemical shifts. As a result, the variation in evolution under time independent interactions is compensated by design.

Radiofrequency field distribution generated in solenoidal coil

In this section, we provide details on the spatial distribution of the rf fields used in our study. We assumed a solenoidal coil with the length of 7.9 mm, diameter of 3.9 mm, and with 7 turns, which represents the typical coil used in the 3.2 mm MAS probes (Bruker) (*12*). The magnetic field of the coil was calculated using a semi-analytical model introduced by Engelke (*55*). It was then converted to the rf field amplitudes and phases presented in Figure S-3 as described in (*12*).
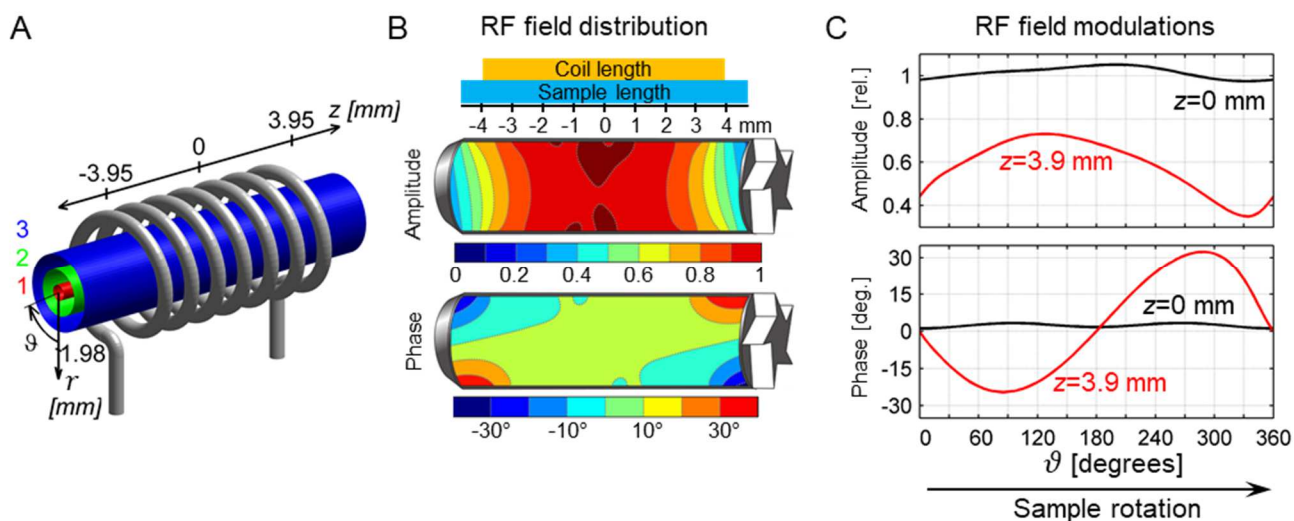
Figure S-3. Illustration of the rf field distribution in a 3.2mm MAS rotor. (A) Definition of coordinates and sample volume elements used in optimal control calculations with compensation of rf field inhomogeneities. (B) Cross-sections through the sample, (z, r) plane for ϑ=[90°,270°], showing the distribution of rf amplitudes and phases. The amplitude at the coil edges (z=3.9 mm) reaches only 50% of the amplitude in the center of the coil, while the phase can vary up to $\pm$30°. When the sample rotates, molecules experience periodical modulations of the rf field due to spatial inhomogeneity as it is depicted in (C) for r=1.5 mm.

Calculation of tm-SPICE pulse sequences

The optimization protocol used to generate tm-SPICE pulse sequences was published in Reference (*15*) and the main features are repeated here for convenience.

To account for the 3D distribution of rf fields in optimal control calculations, the sample volume was divided into elements distributed along the coil axis (7 values to digitize the z-coordinate) in the different cylindrical layers (3 values of the r-coordinate) and over the azimuthal angle ϑ (6 values). The actual values of the x and y components of the rf field are provided in the Supplementary Information of Ref. (*15*) (Tables S-1, S-2 and S-3). To save computation time, the calculation results corresponding to the z-coordinates -0.85 mm and -1.71 mm were assumed to be identical to z=0.85 mm and 1.71 mm, respectively. Under MAS conditions, sample rotation induces periodical changes of the azimuthal angle ϑ which modulates the applied rf pulses. The calculations are repeated independently for different positions within the sample volume – values of z and r, and for initial rotor phases ϑ_0.

The input script for our optimal control calculation is provided further below in this Supplementary Materials as well as the spin system parameters. For generating the tm-SPICE-16.5 sequences, the following parameters were assumed:

proton Larmor frequency: 850MHz
MAS frequency: 16.5 kHz
shaped pulse duration: 60 rotor periods
number of elements in the shapes: 1500
crystal file: ZCW3_144 (the crystal file was adapted from data provided by M.H. Levitt)
spin system: using 4-nuclei sets defined below

The optimization was divided into 3 levels of complexity.

> **Level 1** – an ideal rf field as well as perfect on-resonance conditions were assumed, pulse sequence initiated by random numbers.

> **Level 2** –spatial distribution of rf fields as described above is included while keeping on-resonance conditions. The pulse sequence is initiated by the result of the previous level

> **Level 3** – a spread of chemical shifts is included, digitized using 3 values for the amide nitrogen (-13.4, 0, +13.4 ppm) and using 5 values for the alpha carbon (-12.5, -6.25, 0, +6.25, +12.5 ppm). The range of chemical shifts of the carbonyl carbon was digitized using 3 values (-7.5, 0, +7.5 ppm).

In the final level of the optimization, the calculation was performed on 224 CPUs in parallel and was stopped after 380 optimal control iterations, which took approximately 6 days.

The sequences generated for the numerical survey of the maximal achievable transfer efficiency for the NCA experiment (Figure 2 of the main text) used 2-nuclei spin systems and Level 2 of complexity defined above (no distribution of chemical shifts). Independent runs were used to generate optimal control pulse sequences for each contact time. Calculations were initialized with random values and the algorithm was stopped after 1500 iterations or earlier. This was sufficient to reach high transfer efficiencies. The change of the target function was smaller than 0.001 in the final iterations. Wall times of these calculations were significantly shorter thanks to the smaller spin system and avoiding averaging over chemical shift distributions.

Comparison and parametrization of ramp and adiabatic cross-polarization between ^{15}N and ^{13}C

In this section, we provide details on the numerical study in which we determined the maximal achievable transfer efficiency under conditions reflecting a realistic experimental situation. The results are presented in Figure 2 in the main text.

Ramp-CP

The linear ramp is applied on the ^{13}C channel. In the calculation, the following parameters were optimized for each contact time:

1. ω_N – rf amplitude on the ^{15}N channel, range $\omega_N \in [1,50]$ kHz
2. ω_C – maximal rf amplitude on the ^{13}C channel, range $\omega_C \in [1,50]$ kHz
3. x – linear ramp percentage, range $x \in [50,95]$ %

Adiabatic-CP

The waveform of a tangential shape of length T is given by the following equation

$$\omega_C(t) = \omega_C \left\{ 1 + a \tan \left[\left(\frac{2t}{T} - 1 \right) \arctan \left(\frac{r}{a} \right) \right] \right\}$$

In the experiment, the tangential shape was applied on the ^{13}C channel. In the calculation, the following parameters were optimized for each contact time:

1. ω_N – rf amplitude on the ^{15}N channel, range $\omega_N \in [1,50]$ kHz
2. ω_C – average RF amplitude on the ^{13}C channel, range $\omega_C \in [1,50]$ kHz
3. r – range of tangential sweep, RF amplitude grows from $(1-r)\omega_C$ up to $(1+r)\omega_C$, range $r \in [0.001, 0.999]$
4. a – shape factor of the tangent curve, range $a \in [0.005, 0.5]$
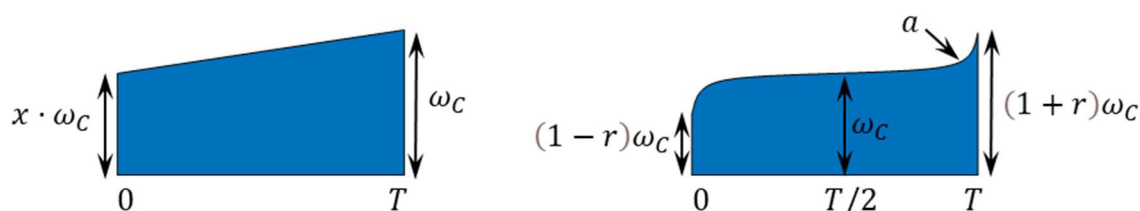
Figure S-4. Definition of parameters used to characterize linear rf ramp (left) and adiabatic tangential pulse shape (right) used in the cross-polarization experiment.

Comparison of shapes

When inspecting the maximal possible transfer in the NCA experiment performed at a MAS frequency of 16.5 kHz (Figure 2 of the main text), we found that the linear rf ramp and the adiabatic tangential pulse shape CP yield the same transfer efficiency. As shown in Figure S-5, their waveforms are quite similar. The linear ramp approximates the tangential shape in its middle part. The minute discrepancies at the beginning and at the end of the tangential shape do not yield significant improvements. Figure S-5 shows how the rf amplitude is swept through the Hartmann-Hahn condition for contact times of 2.42 ms (40 rotor periods), 4.24 ms (70 rotor periods), and 6.06 ms (100 rotor periods). The curves represent the difference between the rf amplitudes applied on the ^{15}N and the ^{13}C channels. This difference should be equal to 16.5 kHz, which corresponds to the MAS frequency. Due to rf inhomogeneity, the difference of mean rf amplitudes is, however, larger for all cases.
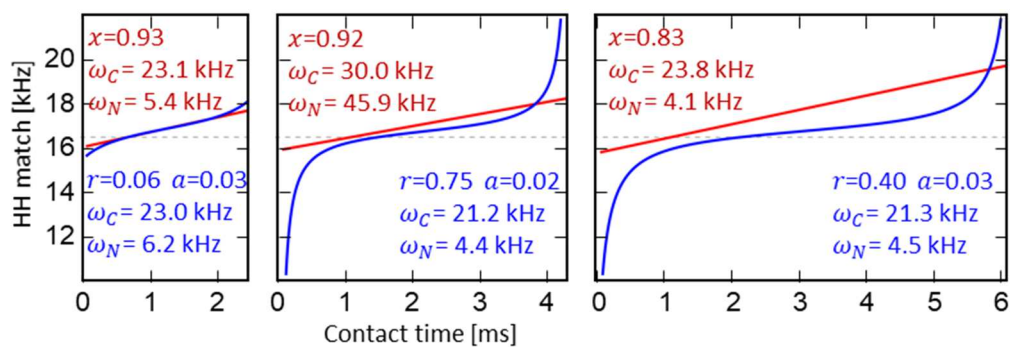
Figure S-5. Comparison of linear rf ramp (red) and adiabatic tangential pulse shape (blue) sweeps in the cross-polarization experiment. The parameters $\{x, \omega_C, \omega_N\}$ and $\{r, a, \omega_C, \omega_N\}$ were optimized individually for contact times 2.42 ms (40 rotor periods), 4.24 ms (70 rotor periods), and 6.06 ms (100 rotor periods) assuming MAS frequency of 16.5 kHz (dashed grey line), spatial rf field inhomogeneity, and NCA transfer conditions.

Cross-polarization between amide ^{1}H-^{15}N spins
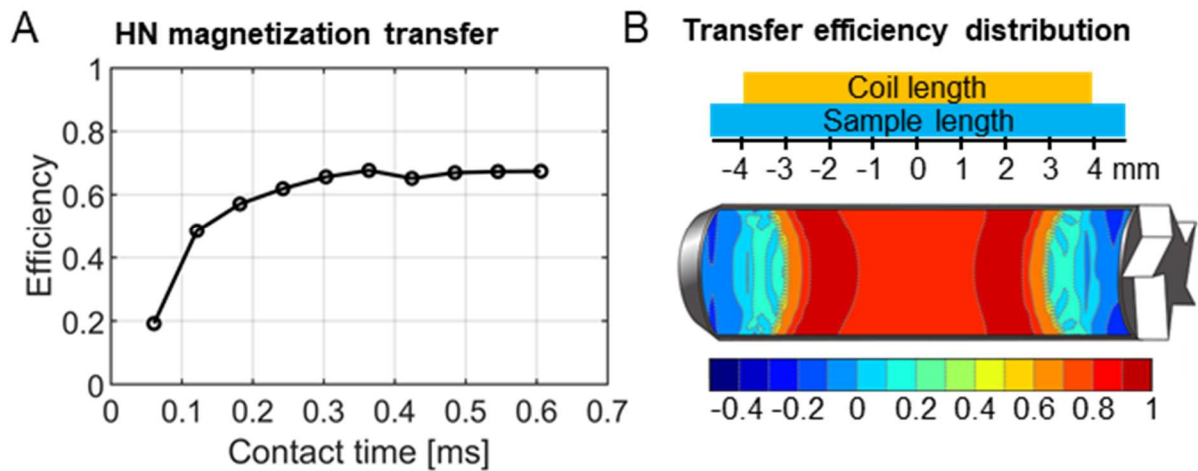
Figure S-6. (A) Top curve – best achievable transfer efficiencies estimated by numerical optimizations of ramp-CP (linear rf ramp 70-100% applied on the ^{1}H channel). Pulse sequence parameters were optimized for each contact time independently. In the calculations, the assumed dipolar coupling and CSA parameters correspond to a ^{1}H-^{15}N spin pair that interacts with a dipolar coupling constant of 10 kHz. The sample is rotated with a MAS frequency of 16.5 kHz, assuming a static magnetic field strength of 700 MHz. (B) Illustration of the spatial distribution of the magnetization transfer efficiency for a ramp-CP optimized for a duration of 6 rotor periods (about 0.36 ms). The large dipolar coupling constant leads to improved robustness towards rf inhomogeneities. Efficient transfer is achieved in a larger volume as compared to the ^{15}N-^{13}C case.

Cross-polarization between ^{15}N and ^{13}Cα or ^{13}C' – mapping recoupling conditions

Here we present the results of numerical calibration of the linear rf ramp CP experiment applied to the NCA and NCO transfers. Figure S-7 complements similar data presented in the main text, Figure 5A.
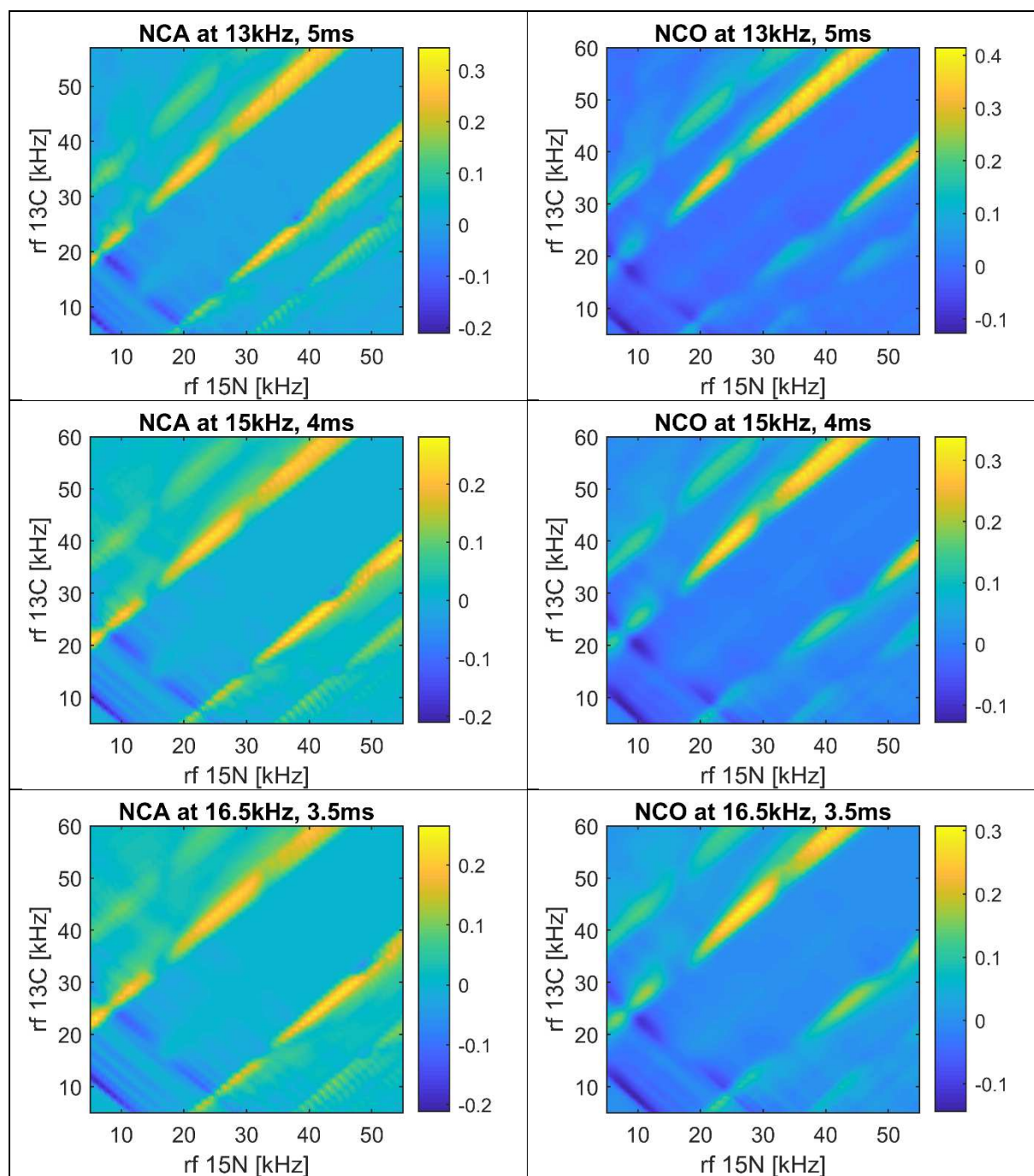
Figure S-7. continued…
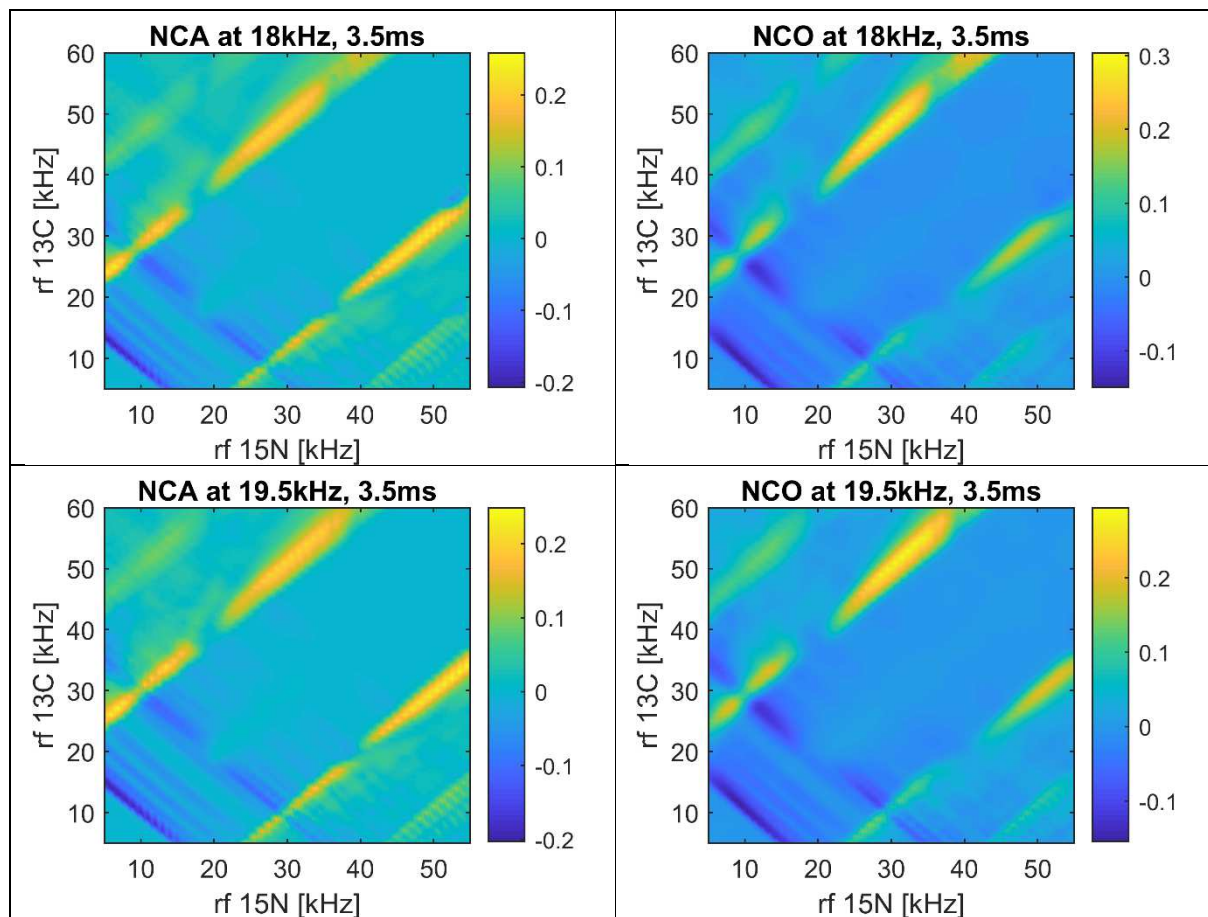
Figure S-7. Transfer efficiencies calculated for NCA and NCO ramp-CP experiments. The calculations were performed over a wide range of rf amplitudes and for MAS frequencies of 13-19.5 kHz indicated in the graph titles. A linear ramp 90-100 % was applied on the ^{13}C channel using the contact times indicated in the graph titles. Calculations assumed a magnetic field of 16.5 T (corresponding to a ^{1}H Larmor frequency of 700 MHz), and a realistic 3D distribution of the rf fields generated by the solenoid coil. The maps can be used to identify appropriate rf parameters for the experiment.

Effect of proton decoupling on transfer efficiency as a function of MAS frequency

Experimentally, we observe a decrease of the signal intensities with increasing MAS frequencies, see Figure 6 of the main text. Using numerical simulations, we explain this by the effect of insufficient proton decoupling during the NCA/NCO transfer.

The spin systems, consisting of 8 nuclei and involving 4 heteroatoms and 4 nearby protons, were derived from the f-MLF structure (PDB entry 1Q7O) focusing on the leucine residue and are depicted in Figure S-8. The tm-SPICE-16.5 pulse sequence was used and rescaled to the corresponding MAS frequency while a fixed amplitude (continuous wave) rf irradiation was applied on the proton channel. For the sake of computation time, the spatial rf inhomogeneity was approximated by a corresponding distribution along the coil axis while rotational modulations were ignored for all 3 rf channels.
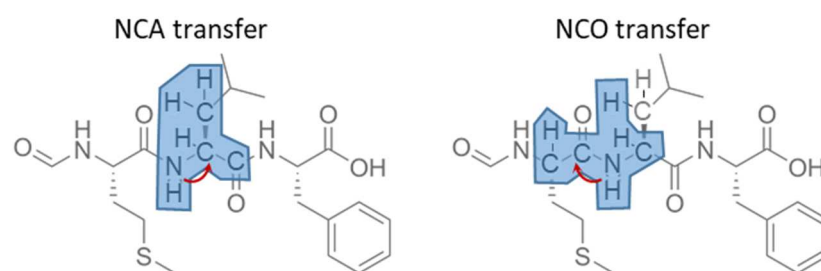
Figure S-8. Definition of the spin systems used to evaluate the influence of insufficient proton decoupling on the NCA/NCO transfer efficiency.

Figure S-9 demonstrates how the NCA/NCO transfer efficiency depends on the proton rf amplitude at different MAS frequencies. Sufficient proton decoupling is achieved using 200 kHz rf amplitude which is out of reach for a typical 3.2 mm MAS probe. At the same time, we observe decreasing performance of the tm-SPICE-16.5 sequence for increasing MAS frequency when the proton rf amplitude is fixed at 85 kHz (used in the experiment). In particular, the numerically predicted NCA transfer efficiency drops by 55% when the MAS frequency is increased from 13 to 19.5 kHz and in the case of the NCO transfer the efficiency decreases by 30%. Table S-1 provides a direct comparison of the relative experimental spectral intensities (integral of all three Cα peaks) with the numerically predicted transfer efficiencies calculated at different MAS frequencies (still assuming 85 kHz proton decoupling used for all MAS frequencies). We observe a fairly good agreement.
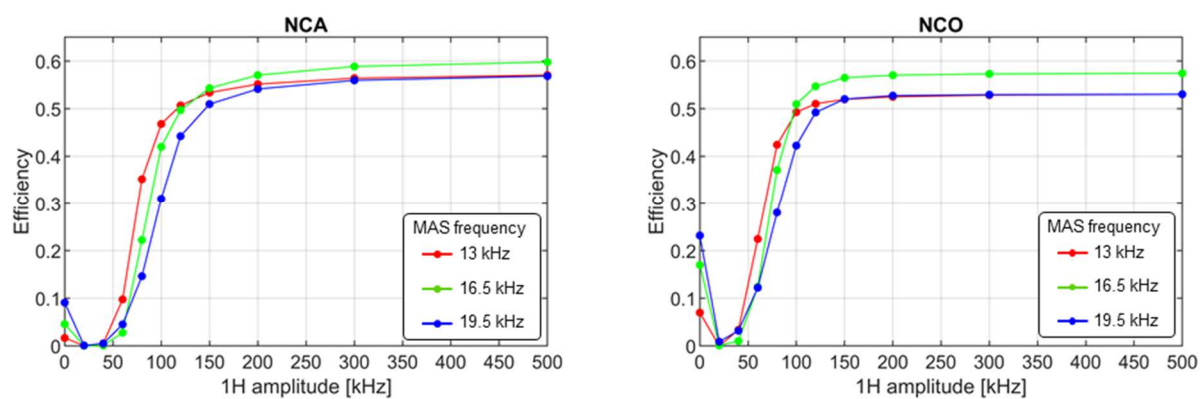
Figure S-9. Transfer efficiency in the NCA (left) and NCO (right) tm-SPICE-16.5 experiments as a function of rf amplitude of the continuous-wave proton (^1H) decoupling, calculated for MAS frequencies of 13, 16.5 and 19.5 kHz.

Table S-1. Relative intensities of the NCA transfer of the tm-SPICE-16.5 sequence as a function of MAS frequency. Simulation accounts for insufficient proton decoupling.

	13 kHz	15 kHz	16.5 kHz	18 kHz	19.5 kHz
experiment	1.00	0.93	0.84	0.72	0.55
simulation	1.00	0.86	0.71	0.58	0.45

Spin-system parameters used in numerical simulations – SIMPSON convention

Simulations of ^{1}H-^{15}N transfer

```
spinsys {
  channels 1H 15N
  nuclei   1H 15N

  shift 1  0p 7.7p 0.65 37.47 84.54 134.52
  shift 2 0p 99p 0.19 103.01 -141.57 65.13
  dipole 1 2 10000.0 0 142.20 -142.56
  jcoupling 1 2 -92 0 0 0 0 0
}
```

Simulations of NCA transfer using 2 spins, ^{15}N-^{13}Cα

```
spinsys {
  channels  15N 13C
  nuclei    15N 13C

  shift 1 0p  99p 0.19 103.01 -141.57 65.13
  shift 2 0p -20p 0.43 -81.06 37.80 37.44
  dipole 1 2 1019.18 0 63.76 113.83
  jcoupling 1 2 -11 0 0 0 0 0
}
```

Simulations of NCO transfer using 2 spins, ^{15}N-^{13}C'

```
spinsys {
  channels 15N 13C
  nuclei   15N 13C

  shift 1 0p  99p 0.19 103.01 -141.57 65.13
  shift 2 0p -76p 0.90 100.87 -127.27 -131.30
  dipole 1 2  1349.5 0 72.69 -27.59
  jcoupling 1 2 -15 0 0 0 0 0
}
```

Optimizations of tm-SPICE NCA transfer using 4 spins,^{13}C'-^{15}N-^{13}Cα-^{13}Cβ

```
spinsys {
  channels  15N 13C
  nuclei    15N 13C 13C 13C

  shift 1  0p  99p 0.19 103.01 -141.57 65.13
  shift 2  0p -20p 0.43 -81.06 37.80 37.44
  shift 3 118.4p -76p 0.90 -150.38 89.66 -24.46
  shift 4 -16.1p -20p 0.43 -81.06 37.80 37.44

  dipole 1 2 1019.1 0 63.76 113.83
  dipole 1 3 224.7 0 92.27 88.65
  dipole 1 4 207.8 0 75.88 149.71
  dipole 2 3 -2153.9 0 61.21 -115.71
```

```
    dipole 2 4 -2119.0 0 88.50 -0.56
    dipole 3 4 -476.3 0 105.97 29.37

    jcoupling 1 2 -11 0 0 0 0 0
    jcoupling 2 3  55 0 0 0 0 0
    jcoupling 2 4  35 0 0 0 0 0
}
```

Optimizations of tm-SPICE NCO transfer using 4 spins, $^{13}C\alpha$-$^{13}C'$-^{15}N-$^{13}C\alpha$

```
spinsys {
  channels 15N 13C
  nuclei   15N 13C 13C 13C

  shift 1 0p 99p 0.19 103.01 -141.57 65.13
  shift 2 0p -76p 0.90 100.87 -127.26 -131.30
  shift 3 -120.2p -20p 0.43 -81.06 37.80 37.44
  shift 4 -115.4p -20p 0.43 -81.06 37.80 37.44

  dipole 1 2  1349.4 0 72.69 -27.58
  dipole 2 4  -537.0 0 95.86 -47.18
  dipole 2 3 -2219.0 0 124.05 -71.46
  dipole 1 4  1019.1 0 63.76 113.83
  dipole 1 3   231.2 0 101.03 -49.47
  dipole 3 4  -144.8 0 106.93 -55.43

  jcoupling 1 2 -15 0 0 0 0 0
  jcoupling 1 3   7 0 0 0 0 0
  jcoupling 1 4 -11 0 0 0 0 0
  jcoupling 2 3  55 0 0 0 0 0
}
```

Simulation of proton decoupling influence on tm-SPICE NCA transfer using 8 spins

```
spinsys {
  channels  15N 13C  1H
  nuclei 15N 13C 13C 13C 1H 1H 1H 1H

  shift 1 0p 99p 0.19 103.01 -141.57 65.13
  shift 2 0p -20p 0.43 -81.06 37.80 37.44
  shift 3 115.4p -76p 0.90 100.87 -127.26 -131.30
  shift 4  -16.1p -10p 0.3 0 0 0
# for 1H shifts, water is assumed on resonance
  shift 5 4.6p 7.7p 0.65 37.46 84.53 134.52
  shift 6 -0.17p  8p 0.5 0 0 0
  shift 7  -2.56p  6p 0.5 0 0 0
  shift 8  -2.56p  6p 0.5 0 0 0

  dipole 1 2 1019.1 0 63.76 113.83
  dipole 1 3 1349.4 0 72.69 -27.58
  dipole 1 4 207.87 0 75.88 149.71
  dipole 1 5 12853.5 0 142.19 -142.55
  dipole 1 6 1395.7 0 35.97 98.51
  dipole 1 7 590.5 0 99.04 150.58
```

```
  dipole 1 8 319.9 0 69.68 139.51
  dipole 2 3 -537.0 0 95.86 -47.18
  dipole 2 4 -2119.0 0 88.50 -0.56
  dipole 2 5 -3268.9 0 47.63 91.66
  dipole 2 6 -23712.0 0 161.48 -178.00
  dipole 2 7 -3128.3 0 59.86 -4.54
  dipole 2 8 -3116.1 0 104.39 -24.72
  dipole 3 4 -157.9 0 93.26 -29.35
  dipole 3 5 -3868.5 0 53.97 -7.70
  dipole 3 6 -1844.2 0 120.13 -54.00
  dipole 3 7 -455.9 0 78.27 -28.83
  dipole 3 8 -341.8 0 100.04 -36.82
  dipole 4 5 -1697.1 0 58.24 135.18
  dipole 4 6 -3010.5 0 119.67 179.90
  dipole 4 7 -23883.3 0 17.92 -23.17
  dipole 4 8 -24013.1 0 121.87 -67.82
  dipole 5 6 -4853.5 0 146.92 -100.83
  dipole 5 7 -7192.7 0 97.75 -42.03
  dipole 5 8 -2477.4 0 122.21 -51.48
  dipole 6 7 -4327.4 0 46.16 -3.51
  dipole 6 8 -8377.0 0 78.17 -20.99
  dipole 7 8 -22288.5 0 155.78 -86.81

  jcoupling 1 2 -11 0 0 0 0 0
  jcoupling 1 3 -15 0 0 0 0 0
  jcoupling 1 5 -92 0 0 0 0 0
  jcoupling 2 4  35 0 0 0 0 0
  jcoupling 2 6 140 0 0 0 0 0
  jcoupling 4 7 140 0 0 0 0 0
  jcoupling 4 8 140 0 0 0 0 0
}
```

Simulation of proton decoupling influence on tm-SPICE NCO transfer using 8 spins

```
spinsys {
  channels 15N 13C 1H
  nuclei 15N 13C 13C 13C 1H 1H 1H 1H

  shift 1 0p 99p 0.19 103.01 -141.57 65.13
  shift 2 0p -76p 0.90 100.87 -127.26 -131.30
  shift 3 -120.2p -20p 0.43 -81.06 67.80 -37.44
  shift 4 -115.4p -20p 0.43 -81.06 37.80 37.44
# for 1H shifts, water is assumed on resonance
  shift 5 4.6p 7.7p 0.65 37.46 84.53 134.52
  shift 6 -0.17p  8p 0.5 0 0 0
  shift 7 -0.22p  8p 0.5 0 0 0
  shift 8  -2.56p  6p 0.5 0 0 0

  dipole 1 2 1349.4 0 72.69 -27.58
  dipole 1 3 231.2 0 101.03 -49.47
  dipole 1 4 1019.1 0 63.76 113.83
  dipole 1 5 12853.5 0 37.80 37.44
  dipole 1 6 1395.7 0 144.02 -81.48
  dipole 1 7 778.4 0 73.69 104.86
```

```
    dipole 1 8 692.4 0 39.65 169.51
    dipole 2 3 -2219.0 0 124.05 -71.46
    dipole 2 4 -537.0 0 95.86 -47.18
    dipole 2 5 -3868.5 0 53.97 -7.70
    dipole 2 6 -1844.2 0 120.13 -54.00
    dipole 2 7 -3202.3 0 58.85 74.08
    dipole 2 8 -2017.8 0 13.85 -151.78
    dipole 3 4 -144.8 0 106.94 -55.43
    dipole 3 5 -2050.6 0 82.42 -35.14
    dipole 3 6 -467.3 0 121.86 -60.31
    dipole 3 7 -23949.7 0 76.67 31.86
    dipole 3 8 -3107.8 0 43.46 -94.80
    dipole 4 5 -3268.9 0 47.63 91.66
    dipole 4 6 -23712.0 0 161.48 -178.00
    dipole 4 7 -501.3 0 70.01 108.00
    dipole 4 8 -587.9 0 44.75 145.41
    dipole 5 6 -4853.5 0 146.92 -100.83
    dipole 5 7 -10678.5 0 88.10 -60.75
    dipole 5 8 -8257.1 0 120.14 1.73
    dipole 6 7 -1497.2 0 123.30 -77.25
    dipole 6 8 -1452.9 0 147.35 -39.59
    dipole 7 8 -6782.3 0 60.08 -116.72

    jcoupling 1 2 -15 0 0 0 0 0
    jcoupling 1 3   7 0 0 0 0 0
    jcoupling 1 4 -11 0 0 0 0 0
    jcoupling 2 3  55 0 0 0 0 0
    jcoupling 1 5 -92 0 0 0 0 0
    jcoupling 3 7 140 0 0 0 0 0
    jcoupling 4 6 140 0 0 0 0 0
}
```

Typical SIMPSON input files

The SIMPSON program that can account for rotation-modulated rf inhomogeneities is available from the web www.optimal-nmr.net. It is still under development and this feature requires a specific setup of the simulation which is not described in the previous SIMPSON papers. In particular, the time step of discretization of a shaped pulse must be smaller than 1/6 of the rotor period. The files containing the parametrization of the rf fields (coil_inhom.dat), as well as the following input files, can be obtained from the web www.optimal-nmr.net or on request from Z.T.

Calculation of transfer efficiency maps – ramp-CP

```
source NCA.spinsys
# or any other text-file containing spinsys section

par {
  method    direct dsyev
  crystal_file zcw3_144
  gamma_angles 1
  rfmap   coil_inhom.dat

  start_operator        I1x
  detect_operator       I2x
  proton_frequency      700e6
  sw                    1e6/100
  np                    1
  num_cores 28
# this is to run on HPC, adjust to your computer's number of cores
}

proc pulseq {} {
    global par shN shC

    maxdt $par(maxdt)
    pulse_shaped_rotormodulated $par(dur) $shN  $shC
    acq
}

proc main {} {
  global par shN shC

  if {[llength $::argv] != 3} {
    puts stderr "Usage: simpson $par(name).in <MAS kHz> <dur us>\n"
    exit
  }
  set mas [lindex $::argv 1]
  set par(spin_rate) [expr $mas*1000]
  set par(dur) [lindex $::argv 2]
  set par(maxdt) [expr 1.0e6/$par(spin_rate)/16]
  set Nelem 1000

  set fn [open $par(name)_$mas\_dur_$par(dur)_results.txt w]
  puts $fn " rfN(const)      rfC(ramp 90-100)      eff "

  for {set rfC 5000} {$rfC<=60000} {incr rfC 1000} {
```

```
            set par(rfC) [expr $rfC*1.0]
            set shC [shape_create $Nelem -ampl {$par(rfC)*(0.9+0.1*($i-1)/$Nelem)}]
            for {set rfN 5000} {$rfN<=55000} {incr rfN 250} {
                set par(rfN) [expr $rfN*1.0]
                set shN [shape_create $Nelem -ampl $par(rfN)]
                set f [fsimpson]
                set vals [findex $f 1 -re]
                funload $f
                puts $fn "[format "%10.0f" $par(rfN)] [format "%10.0f" $par(rfC)]  $vals"
                free_shape $shN
            }
            free_shape $shC
            flush $fn
    }
    close $fn
}
```

Calculation of tm-SPICE-16.5 sequence

```
# ZERO QUANTUM transfer, little RF energy penalty and hard RF limits

source NCACOcCB.spinsys
# or any other text-file containing spinsys section

par {
  num_cores 1
  # this calculation is distributed over multiple cores using MPI protocol

  method    direct dsyev
  crystal_file zcw3_144.cry
  gamma_angles 1
  spin_rate    16500
  start_operator      I1x
  detect_operator     I2x
  proton_frequency    850e6
  sw                  1e6

  variable Nspins 4
  variable recalc pow(2,2-Nspins)
  # define number of spins and calculate normalization factor

  oc_method CG
  oc_grad_level 2
  oc_var_save_proc rfstore
  conjugate_fid false
  # optimal control related parameters
}

# procedure to store rf shape(s) during oc_optimize and to monitor convergence
proc rfstore {} {
  global par rfsh1 rfsh2 optname itercount fout tfcomponents

  incr itercount $par(oc_var_save_iter)
  save_shape $rfsh1 $optname\_N_temp_$itercount.dat
```

```
    save_shape $rfsh2 $optname\_C_temp_$itercount.dat
    puts $fout "Iter $itercount : $tfcomponents"
    flush $fout
}

# pulse sequence when ignoring rf temporal modulations
proc pulseq_OC {} {
  global par rfsh1 rfsh2

  maxdt $par(maxdt)
  reset
  pulse_shaped $par(duration) $rfsh1 $rfsh2
  oc_acq_hermit
}

# pulse sequence which includes rf temporal modulations
proc pulseq_OC_rotmod {} {
  global par rfsh1 rfsh2

  maxdt $par(maxdt)
  reset
  pulse_shaped_rotormodulated $par(duration) $rfsh1 $rfsh2
  oc_acq_hermit
}

# optimal control target function
proc target_function {} {
  global par rfsh1 rfsh2

  set par(np) 1
  set f [fsimpson]
  set Res [expr [findex $f 1 -re]*$par(recalc) ]
  funload $f
  set pen1 [expr $par(lamN)*[shape_energy $rfsh1 $par(duration)]]
  set pen2 [expr $par(lamC)*[shape_energy $rfsh2 $par(duration)]]
  set Res [expr $Res - $pen1 - $pen2]
  return [format "%.20f" $Res]
}

# optimal control gradients, hidden variable $par(_phivals_) contains
#    target_function value calculated along
proc gradient {} {
  global par rfsh1 rfsh2  tfcomponents

  # FID length with gradients is 2channels x number-of-elements-in-shape
  set par(np) [expr 2*$par(Norig) ]
  # looping over offset profiles is done in averaging_file (if defined)
  set f [fsimpson]
  fscale $f -scale $par(recalc)
  oc_grad_add_energy_penalty $f $rfsh1 -$par(lamN) $rfsh2 -$par(lamC)
  set pen1 [expr $par(lamN)*[shape_energy $rfsh1 $par(duration)]]
  set pen2 [expr $par(lamC)*[shape_energy $rfsh2 $par(duration)]]
  set tfcomponents [list [expr $par(_phivals_)*$par(recalc)] $pen1 $pen2 ]
  return $f
}
```

```
# generates list of control-point numbers distributed over +/-SW/2 range
proc get_lims {SWH cp} {
  if { $cp <= 1} {
    set Res 0
  } else {
    set step [expr double($SWH)/($cp-1)]
    set Res {}
    for {set i 0} {$i < $cp} {incr i} {
      set shft [expr double($SWH)/2.0-$i*$step]
      lappend Res $shft
    }
  }
  return $Res
}

# preparing averaging file (over isotropic shifts)
proc prepare_ave {vals1 vals2 filename} {
  set fd [open $filename w]
  puts $fd "shift_1_iso shift_2_iso weight"
  set w [expr 1.0 / ([llength $vals1] * [llength $vals2]) ]
  foreach a $vals1 {
    foreach b $vals2 {
      puts $fd "[format "%8.2f" $a]p [format "%8.2f" $b]p [format "%12.8f" $w]"
    }
  }
  close $fd
}

proc main {} {
  global par rfsh1 rfsh2 limsC limsN optname itercount fout tfcomponents

  set number_of_rotor_periods 60
  set taur [expr 1.0e6/$par(spin_rate)]
  set par(duration) [expr $number_of_rotor_periods*$taur]
  set pulses_per_period  25
  set par(Norig) [expr $number_of_rotor_periods*$pulses_per_period]
  set tfcomponents [list 0.0 0.0 0.0]
  set par(lamN) 3e-11
  set par(lamC) 1e-11
  set par(maxdt)  3
  set par(levN) 35000
  set par(levC) 35000

  # level 1
  set rfsh1 [rand_shape 5000 $par(Norig) [expr int($number_of_rotor_periods/2)] ]
  set rfsh2 [rand_shape 5000 $par(Norig) [expr int($number_of_rotor_periods/2)] ]
  set optname shape_lev1
  set fout [open $optname\_output.txt w]
  set par(oc_var_save_iter) 30
  set par(pulse_sequence) pulseq_OC
  set itercount 0
  set par(oc_max_iter) 150
  set tfopt [oc_optimize $rfsh1 -max $par(levN) $rfsh2 -max $par(levC)]
  save_shape $rfsh1 $optname\_final_N.dat
```

```
    save_shape $rfsh2 $optname\_final_C.dat
    close $fout

    # level 2
    set optname shape_lev2
    set fout [open $optname\_output.txt w]
    set par(rfmap) coil_inhom.dat
    # adds rf modulations in, need to change pulse sequence as well
    set par(pulse_sequence) pulseq_OC_rotmod
    set itercount 0
    set par(oc_var_save_iter) 5
    set par(oc_max_iter) 500
    set tfopt [oc_optimize $rfsh1 -max $par(levN) $rfsh2 -max $par(levC)]
    save_shape $rfsh1 $optname\_final_N.dat
    save_shape $rfsh2 $optname\_final_C.dat
    close $fout

    # level 3
    set optname shape_lev3
    set fout [open $optname\_output.txt a]
    # add averaging over distribution of chemical shifts by defining averaging_file
    set limsN [get_lims 26.8 3]
    set limsC [get_lims 25 5]
    set par(averaging_file) $par(name).ave
    prepare_ave $limsN $limsC $par(averaging_file)
    set itercount 0
    set par(oc_var_save_iter) 5
    set par(oc_max_iter) 500
    set tfopt [oc_optimize $rfsh1 -max $par(levN) $rfsh2 -max $par(levC)]
    save_shape $rfsh1 $optname\_final_N.dat
    save_shape $rfsh2 $optname\_final_C.dat
    close $fout

    free_all_shapes
}
```

Tm-SPICE shaped pulses files

We provide data files of the tm-SPICE-16.5 and tm-SPICE-20 NCA and NCO experiments in the Bruker wave format which can be directly used on the Bruker NMR spectrometers. These files can be downloaded from the publisher website or from www.optimal-nmr.net .

Data S1. tmSPICE-MAS16.5kHz-NCA.zip - tm-SPICE shaped pulses for the NCA experiment optimized for the MAS frequency of 16.5 kHz and the duration of 60 rotor periods. Maximal rf amplitude set to 35 kHz on both channels, mean rf amplitude is 10/15 kHz on the $^{13}C/^{15}N$ channels.

Data S2. tmSPICE-MAS16.5kHz-NCO.zip - tm-SPICE shaped pulses for the NCO experiment optimized for the MAS frequency of 16.5 kHz and the duration of 60 rotor periods. Maximal rf amplitude set to 35 kHz on both channels, mean rf amplitude is 10/15 kHz on the $^{13}C/^{15}N$ channels.

Data S3. tmSPICE-MAS20kHz-NCA.zip - tm-SPICE shaped pulses for the NCA experiment optimized for the MAS frequency of 20 kHz and the duration of 70 rotor periods. Maximal rf amplitude set to 40 kHz on both channels, mean rf amplitude is 10 kHz on the both $^{13}C/^{15}N$ channels.

Data S4. tmSPICE-MAS20kHz-NCO.zip - tm-SPICE shaped pulses for the NCO experiment optimized for the MAS frequency of 20 kHz and the duration of 70 rotor periods. Maximal rf amplitude set to 40 kHz on both channels, mean rf amplitude is 10 kHz on the both $^{13}C/^{15}N$ channels.
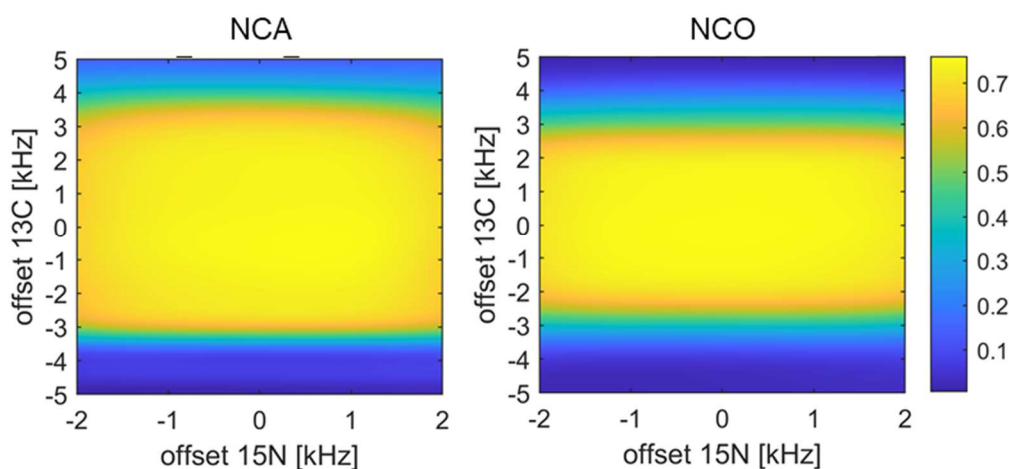
Figure S-10. Transfer efficiency of tm-SPICE-16.5 NCA/NCO experiments calculated over a range of chemical shift offsets. In both cases, a flat profile is obtained over the desired region.

REFERENCES AND NOTES

1. B. Reif, S. E. Ashbrook, L. Emsley, M. Hong, Solid-state NMR spectroscopy. *Nat. Rev. Methods Prim.* **1**, 2 (2021).

2. M. A. Wälti, F. Ravotti, H. Arai, C. G. Glabe, J. S. Wall, A. Böckmann, P. Güntert, B. H. Meier, R. Riek, Atomic-resolution structure of a disease-relevant Aβ(1-42) amyloid fibril. *Proc. Natl. Acad. Sci. U.S.A.* **113**, E4976-E4984 (2016).

3. M. D. Tuttle, G. Comellas, A. J. Nieuwkoop, D. J. Covell, D. A. Berthold, K. D. Kloepper, J. M. Courtney, J. K. Kim, A. M. Barclay, A. Kendall, W. Wan, G. Stubbs, C. D. Schwieters, V. M. Y. Lee, J. M. George, C. M. Rienstra, Solid-state NMR structure of a pathogenic fibril of full-length human α-synuclein. *Nat. Struct. Mol. Biol.* **23**, 409–415 (2016).

4. A. E. McDermott, Structural and dynamic studies of proteins by solid-state NMR spectroscopy: Rapid movement forward. *Curr. Opin. Struct. Biol.* **14**, 554–561 (2004).

5. J. Schaefer, R. A. McKay, E. O. Stejskal, Double-cross-polarization NMR of solids. *J. Magn. Reson.* **34**, 443–447 (1979).

6. S. R. Hartmann, E. L. Hahn, Nuclear double resonance in the rotating frame. *Phys. Rev.* **128**, 2042–2053 (1962).

7. E. O. Stejskal, J. Schaefer, J. S. Waugh, Magic-angle spinning and polarization transfer in proton-enhanced NMR. *J. Magn. Reson.* **28**, 105–112 (1977).

8. G. Metz, X. L. Wu, S. O. Smith, Ramped-amplitude cross polarization in magic-angle-spinning NMR. *J. Magn. Reson. Ser. A.* **110**, 219–227 (1994).

9. M. Baldus, D. G. Geurts, S. Hediger, B. H. Meier, Efficient ^{15}N–^{13}C polarization transfer by adiabatic-passage Hartmann-Hahn cross polarization. *J. Magn. Reson. Ser. A.* **118**, 140–144 (1996).

10. O. B. Peersen, X. L. Wu, S. O. Smith, Enhancement of CP-MAS signals by variable-amplitude cross polarization. Compensation for inhomogeneous B1 fields. *J. Magn. Reson. Ser. A.* **106**, 127–131 (1994).

11. R. Gupta, G. Hou, T. Polenova, A. J. Vega, RF inhomogeneity and how it controls CPMAS. *Solid State Nucl. Magn. Reson.* **72**, 17–26 (2015).

12. Z. Tošner, A. Purea, J. O. Struppe, S. Wegner, F. Engelke, S. J. Glaser, B. Reif, Radiofrequency fields in MAS solid state NMR probes. *J. Magn. Reson.* **284**, 20–32 (2017).

13. T. G. Oas, R. G. Griffin, M. H. Levitt, Rotary resonance recoupling of dipolar interactions in solid-state nuclear magnetic resonance spectroscopy. *J. Chem. Phys.* **89**, 692–695 (1988).

14. M. H. Levitt, T. G. Oas, R. G. Griffin, Rotary resonance recoupling in heteronuclear spin pair systems. *Isr. J. Chem.* **28**, 271–282 (1988).

15. Z. Tošner, R. Sarkar, J. Becker-Baldus, C. Glaubitz, S. Wegner, F. Engelke, S. J. Glaser, B. Reif, Overcoming volume selectivity of dipolar recoupling in biological solid-state NMR spectroscopy. *Angew. Chemie - Int. Ed.* **57**, 14514–14518 (2018).

16. K. Aebischer, Z. Tošner, M. Ernst, Effects of radial radio-frequency field inhomogeneity on MAS solid-state NMR experiments. *Magn. Reson.* **2**, 523–543 (2021).

17. U. Haeberlen, J. S. Waugh, Coherent averaging effects in magnetic resonance. *Phys. Rev.* **175**, 453–467 (1968).

18. A. Schmidt, S. Vega, The Floquet theory of nuclear magnetic resonance spectroscopy of single spins and dipolar coupled spin pairs in rotating solids. *J. Chem. Phys.* **96**, 2655–2680 (1992).

19. N. Khaneja, T. Reiss, C. Kehlet, T. Schulte-Herbruggen, S. J. Glaser, Optimal control of coupled spin dynamics: Design of NMR pulse sequences by gradient ascent algorithms. *J. Magn. Reson.* **172**, 296–305 (2005).

20. N. C. Nielsen, C. Kehlet, S. J. Glaser, N. Khaneja, in *eMagRes* (John Wiley & Sons, 2007); http://dx.doi.org/10.1002/9780470034590.emrstm1043.

21. S. J. Glaser, U. Boscain, T. Calarco, C. P. Koch, W. Köckenberger, R. Kosloff, I. Kuprov, B. Luy, S. Schirmer, T. Schulte-Herbrüggen, D. Sugny, F. K. Wilhelm, Training Schrödinger's cat:

Quantum optimal control: Strategic report on current status, visions and goals for research in Europe. *Eur. Phys. J. D.* **69**, 279 (2015).

22. P. de Fouquieres, S. G. Schirmer, S. J. Glaser, I. Kuprov, Second order gradient ascent pulse engineering. *J. Magn. Reson.* **212**, 412–417 (2011).

23. T. Vosegaard, C. Kehlet, N. Khaneja, S. J. Glaser, N. C. Nielsen, Improved excitation schemes for multiple-quantum magic-angle spinning for quadrupolar nuclei designed using optimal control theory. *J. Am. Chem. Soc.* **127**, 13768–13769 (2005).

24. N. M. Loening, B.-J. van Rossum, H. Oschkinat, Broadband excitation pulses for high-field solid-state nuclear magnetic resonance spectroscopy. *Magn. Reson. Chem.* **50**, 284–288 (2012).

25. D. Wei, U. Akbey, B. Paaske, H. Oschkinat, B. Reif, M. Bjerring, N. C. Nielsen, Optimal ^{2}H rf pulses and ^{2}H–^{13}C cross-polarization methods for solid-state ^{2}H MAS NMR of perdeuterated proteins. *J. Phys. Chem. Lett.* **2**, 1289–1294 (2011).

26. C. T. Kehlet, A. C. Sivertsen, M. Bjerring, T. O. Reiss, N. Khaneja, S. J. Glaser, N. C. Nielsen, Improving solid-state NMR dipolar recoupling by optimal control. *J. Am. Chem. Soc.* **126**, 10202–10203 (2004).

27. C. Kehlet, T. Vosegaard, N. Khaneja, S. J. Glaser, N. C. Nielsen, Low-power homonuclear dipolar recoupling in solid-state NMR developed using optimal control theory. *Chem. Phys. Lett.* **414**, 204–209 (2005).

28. J. O. Hansen, C. Kehlet, M. Bjerring, T. Vosegaard, S. J. Glaser, N. Khaneja, N. C. Nielsen, Optimal control based design of composite dipolar recoupling experiments by analogy to single-spin inversion pulses. *Chem. Phys. Lett.* **447**, 154–161 (2007).

29. A. B. Nielsen, M. Bjerring, J. T. Nielsen, N. C. Nielsen, Symmetry-based dipolar recoupling by optimal control: Band-selective experiments for assignment of solid-state NMR spectra of proteins. *J. Chem. Phys.* **131**, 025101 (2009).

30. M. Bjerring, S. Jain, B. Paaske, J. M. Vinther, N. C. Nielsen, Designing dipolar recoupling and decoupling experiments for biological solid-state NMR using interleaved continuous wave and rf pulse irradiation. *Acc. Chem. Res.* **46**, 2098–2107 (2013).

31. Z. Tošner, S. J. Glaser, N. Khaneja, N. C. Nielsen, Effective Hamiltonians by optimal control: Solid-state NMR double-quantum planar and isotropic dipolar recoupling. *J. Chem. Phys.* **125,** 184502 (2006).

32. C. Kehlet, M. Bjerring, A. C. Sivertsen, T. Kristensen, J. J. Enghild, S. J. Glaser, N. Khaneja, N. C. Nielsen, Optimal control based NCO and NCA experiments for spectral assignment in biological solid-state NMR spectroscopy. *J. Magn. Reson.* **188**, 216–230 (2007).

33. N. M. Loening, M. Bjerring, N. C. Nielsen, H. Oschkinat, A comparison of NCO and NCA transfer methods for biological solid-state NMR spectroscopy. *J. Magn. Reson.* **214**, 81–90 (2012).

34. D. O. Brunner, K. P. Pruessmann, B_1^+ interferometry for the calibration of RF transmitter arrays. *Magn. Reson. Med.* **61**, 1480–1488 (2009).

35. M. Lapert, Y. Zhang, M. A. Janich, S. J. Glaser, D. Sugny, Exploring the physical limits of saturation contrast in magnetic resonance imaging. *Sci. Rep.* **2**, 589 (2012).

36. D. P. Raleigh, M. H. Levitt, R. G. Griffin, Rotational resonance in solid state NMR. *Chem. Phys. Lett.* **146**, 71–76 (1988).

37. T. Gullion, J. Schaefer, Rotational-echo double-resonance NMR. *J. Magn. Reson.* **81**, 196–200 (1989).

38. Y. K. Lee, N. D. Kurur, M. Helmle, O. G. Johannessen, N. C. Nielsen, M. H. Levitt, Efficient dipolar recoupling in the NMR of rotating solids. A sevenfold symmetric radiofrequency pulse sequence. *Chem. Phys. Lett.* **242**, 304–309 (1995).

39. M. H. Levitt, Symmetry-based pulse sequences in magic-angle spinning solid-state NMR, in *eMagRes* (2007); https://doi.org/10.1002/9780470034590.emrstm0551.

40. S. J. Glaser, T. Schulte-Herbruggen, M. Sieveking, O. Schedletzky, N. C. Nielsen, O. W. Sorensen, C. Griesinger, Unitary control in quantum ensembles: Maximizing signal intensity in coherent spectroscopy. *Science* **280**, 421–424 (1998).

41. Z. Tosner, T. Vosegaard, C. Kehlet, N. Khaneja, S. J. Glaser, N. C. Nielsen, Optimal control in NMR spectroscopy: Numerical implementation in SIMPSON. *J. Magn. Reson.* **197**, 120–134 (2009).

42. B. Dillmann, K. Elbayed, H. Zeiger, M. C. Weingertner, M. Piotto, F. Engelke, A novel low-E field coil to minimize heating of biological samples in solid-state multinuclear NMR experiments. *J. Magn. Reson.* **187**, 10–18 (2007).

43. T. Pradhan, K. Annamalai, R. Sarkar, S. Huhn, U. Hegenbart, S. Schönland, M. Faendrich, B. Reif, Seeded fibrils of the germline variant of human λ-III immunoglobulin light chain FOR005 have a similar core as patient fibrils with reduced stability. *J. Biol. Chem.* **295**, 18474–18484 (2020).

44. T. Pradhan, K. Annamalai, R. Sarkar, U. Hegenbart, S. Schönland, M. Faendrich, B. Reif, Solid state NMR assignments of a human λ-III immunoglobulin light chain amyloid fibril. *Biomol. NMR Assign.* **15**, 9–16 (2021).

45. Z. Niu, R. Sarkar, M. Aichler, H.-J. Wester, B. H. Yousefi, B. Reif, Mapping the binding interface of PET tracer molecules and Alzheimer disease Aβ fibrils by using MAS solid-state NMR spectroscopy. *Chembiochem* **21**, 2495–2502 (2020).

46. M. Bak, J. T. Rasmussen, N. C. Nielsen, SIMPSON: A general simulation program for solid-state NMR spectroscopy. *J. Magn. Reson.* **147**, 296–330 (2000).

47. Z. Tošner, R. Andersen, B. Stevenss, M. Eden, N. C. Nielsen, T. Vosegaard, B. Stevensson, M. Eden, N. C. Nielsen, T. Vosegaard, Computer-intensive simulation of solid-state NMR experiments using SIMPSON. *J. Magn. Reson.* **246**, 79–93 (2014).

48. M. Bak, R. Schultz, T. Vosegaard, N. C. Nielsen, Specification and visualization of anisotropic interaction tensors in polypeptides and numerical simulations in biological solid-state NMR. *J. Magn. Reson.* **154**, 28–45 (2002).

49. V. B. Cheng, H. H. Suzukawa Jr., M. Wolfsberg, Investigations of a nonrandom numerical method for multidimensional integration. *J. Chem. Phys.* **59**, 3992–3999 (1973).

50. A. Equbal, M. Bjerring, P. K. Madhu, N. C. Nielsen, Improving spectral resolution in biological solid-state NMR using phase-alternated rCW heteronuclear decoupling. *Chem. Phys. Lett.* **635**, 339–344 (2015).

51. M. Mehring, *Principles of High Resolution NMR in Solids* (Springer, 1983).

52. M. H. Levitt, M. Edén, Numerical simulation of periodic nuclear magnetic resonance problems: Fast calculation of carousel averages. *Mol. Phys.* **95**, 879–890 (1998).

53. P. Hodgkinson, L. Emsley, Numerical simulation of solid-state NMR experiments. *Prog. Nucl. Magn. Reson. Spectrosc.* **36**, 201–239 (2000).

54. D. L. Goodwin, "Advanced optimal control methods for spin systems," thesis, University of Southampton (2017).

55. F. Engelke, Electromagnetic wave compression and radio frequency homogeneity in NMR solenoidal coils: Computational approach. *Concepts Magn. Reson.* **15**, 129–155 (2002).